Time-Resolved Fuel Density Profiles of the Stagnation Phase of Indirect-Drive Inertial Confinement Implosions

Riccardo Tommasini [1,*] O. L. Landen,[1] L. Berzak Hopkins,[1] S. P. Hatchett,[1] D. H. Kalantar,[1] W. W. Hsing,[1] D. A. Alessi,[1] S. L. Ayers,[1] S. D. Bhandarkar,[1] M. W. Bowers,[1] D. K. Bradley,[1] A. D. Conder,[1] J. M. Di Nicola,[1] P. Di Nicola,[1] L. Divol,[1] D. Fittinghoff,[1] G. Gururangan,[1] G. N. Hall,[1] M. Hamamoto,[1] D. R. Hargrove,[1] E. P. Hartouni,[1] J. E. Heebner,[1] S. I. Herriot,[1] M. R. Hermann,[1] J. P. Holder,[1] D. M. Holunga,[1] D. Homoelle,[1] C. A. Iglesias,[1] N. Izumi,[1] A. J. Kemp,[1] T. Kohut,[1] J. J. Kroll,[1] K. LaFortune,[1] J. K. Lawson,[1] R. Lowe-Webb,[1] A. J. MacKinnon,[1] D. Martinez,[1] N. D. Masters,[1] M. P. Mauldin,[2] J. Milovich,[1] A. Nikroo,[1] J. K. Okui,[1] J. Park,[1] M. Prantil,[1] L. J. Pelz,[1] M. Schoff,[2] R. Sigurdsson,[1] P. L. Volegov,[3] S. Vonhof,[2] T. L. Zobrist,[1] R. J. Wallace,[1] C. F. Walters,[1] P. Wegner,[1] C. Widmayer,[1] W. H. Williams,[1] K. Youngblood,[1,2] M. J. Edwards,[1] and M. C. Herrmann[1]

[1]Lawrence Livermore National Laboratory, 7000 East Avenue, Livermore, California 94550, USA
[2]General Atomics, San Diego, California 92186, USA
[3]Los Alamos National Laboratory, Los Alamos, New Mexico 87545, USA

The implosion efficiency in inertial confinement fusion depends on the degree of stagnated fuel compression, density uniformity, sphericity, and minimum residual kinetic energy achieved. Compton scattering-mediated 50–200 keV x-ray radiographs of indirect-drive cryogenic implosions at the National Ignition Facility capture the dynamic evolution of the fuel as it goes through peak compression, revealing low-mode 3D nonuniformities and thicker fuel with lower peak density than simulated. By differencing two radiographs taken at different times during the same implosion, we also measure the residual kinetic energy not transferred to the hot spot and quantify its impact on the implosion performance.

In inertial confinement fusion, a cryogenic layer of DT fuel is imploded around a gaseous lower density hot spot, with the goal of transferring enough of its kinetic energy to hot-spot internal energy to achieve ignition[1]. The implosion efficiency depends on the degree of stagnated fuel compression, density uniformity, and sphericity achieved [2,3]. Asymmetries are a limiting factor in the minimum achievable volume, since they lead to asynchrony of compression, and additional degrees of freedom through which the kinetic energy, that would otherwise be used in hot-spot heating, can dissipate. At the National Ignition Facility (NIF) [4], the x rays, generated by illuminating the inside of a gold hohlraum[5,6] with 192 laser beams, drive the implosion by the pressure produced from the soft x-ray ablation of a spherical, thin, low-Z capsule, i.e., the ablator, encasing the DT fuel.

Imaging of downscattered neutrons[7] can be used to infer the cold fuel density profile, however, the technique is complicated by sampling only ≈ 1 steradian due to energy-dependent scattering kinematics. Besides requiring deconvolution by the primary neutron source size, typically 50 μm in width, it is sensitive to micron-level uncertainties in relative registration of primary and downscattered images and by definition is burn averaged [8]. Indeed, while x-ray self-emission and neutron imaging [9] have shown the hot-spot symmetry can be controlled to a few percent out of

round, arrays of neutron energy sensitive activation detectors [10] and neutron down-scattered images [8,11,12] indicate that the fuel still suffers from strong asymmetries. Also, experiments performed at the NIF have reported average values of the fuel areal density, which is directly related to the degree of compression, often lower than simulated [13]. Understanding whether the reasons for low compression are 1D in nature (e.g., EOS or shock timing issues) or 3D (hydroinstability growth) is paramount.

Direct, time-resolved, radiography of the ablator and fuel surrounding the hot spot going through maximum compression is fundamental to understanding the degradation mechanisms and how they affect the implosion efficiency. Such a task is challenging as the fuel, a mix of hydrogen isotopes, has a photoabsorption cross section more than 3 orders of magnitude lower than the surrounding carbon-based ablator, and therefore is effectively transparent to traditional techniques. Rather, radiographs equally sensitive to the stagnated fuel and ablator can be obtained using high energy (>50 keV) Compton scattering off its bound and free electrons [14]. In this region, the total "opacity" is dominated by the Compton component: $\kappa_{KN} = \sigma_{KN} N_A Z/A$ (σ_{KN} being the Klein-Nishina cross section [15], Z the total number of free and bound electrons, A the atomic mass, and N_A Avogadro's number). The opacity is insensitive to photon energy, allowing broadband sources and detection, and

almost independent of temperature and density as corrections due to Pauli blocking and the free-free absorption contribution can be shown to be minimal even for the extreme conditions reachable by the stagnated fuel, densities >1000 g/cm³, and partial Fermi degeneracy (temperature T 20%–40% of the Fermi temperature) [16]. This allows accurate inferences of density, in contrast to photoabsorption radiography for which large differences between cold and warm ($T > 50$ eV) opacity, due to removal of K shell electrons, are to be expected and prevent disentangling opacity from density. The high-energy x rays also minimize refractive blurring due to steep density gradients ($>10^{25}$ electrons/cm³/μm) and allow for effective high-pass filtering of backgrounds below 40 keV, such as from the $kT_e \approx 5$ keV hohlraum laser-plasmas and hot-spot emission. A proof of principle of radiography by Compton scattering off room temperature gas-filled direct-drive CH implosions was demonstrated previously at the combined Omega and Omega EP facility [14]. Compton scattering-mediated radiography can greatly benefit other fields of high-energy density physics. Opacity or equation-of-state measurements using radiography [17] could improve in accuracy from disentangling density and areal density from temperature dependencies in the opacity.

In this Letter, we report the first Compton radiographs of stagnated fuel and ablator electron density and hence material density profiles in near ignition scale indirect-drive cryogenically layered implosions. The radiographs provide a wealth of new information on low-mode [18] 3D nonuniformities, lower than simulated peak densities and thicker than expected remaining shell material, attributed to low-mode drive asymmetries and higher-mode hydroinstabilities. By recording multiple images on the same shot around bang time (BT), the evolution of the average fuel radius, asymmetries, and nonuniformities are used to infer the undesirable residual kinetic energy fraction of the system at BT and hence the expected loss of fusion yield.

The experiment setup is shown in Fig. 1. The implosions conducted at the NIF used a three-shock 6-ns-long laser pulse to drive a 5.75-mm-diameter hohlraum containing a suspended capsule of inside radius 845 μm with a 64-μm-thick high-density carbon ablator. The ablator

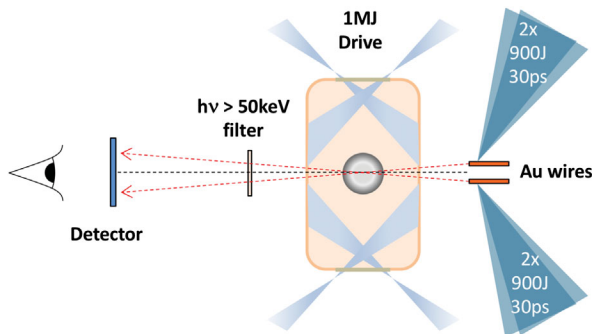contains a 18-μm-thick, 0.25% W-doped layer, starting at 5 μm from the inner radius and encloses a 53-μm-thick cryogenic hydrogen isotope fuel layer [19]. To minimize the backgrounds from DT neutrons, the cryogenic layer used a surrogate tritium-hydrogen mix in a ratio of 3∶1, with a nominal deuterium fraction of 0.2%, maintaining hydroequivalence to usual 50/50 DT layers [20]. The NIF drive pulse delivered a total energy of 1.0 MJ at 3ω (0.35 μm) with a peak power of 400 TW.

The >50 keV point projection backlighters [21] are generated by illuminating two Au wires with four 900 J/30 ps 1ω (1.05 μm) pulses from the Advanced Radiographic Capability (ARC) laser at the NIF facility [22–24], two on each wire. The wires are surrounded by V-shaped plastic structures that reduce signal sensitivity to ARC beam transverse misalignment and enhance the laser-wire coupling by refraction at the plasma mirror surface generated by the ARC prepulse.

The ARC laser beams originate from the chirped-pulse amplification and recompression of an upper 45° NIF quad. Top-down symmetry is recovered by not using the corresponding lower 45° NIF quad. To avoid a 2.5% level mode-1 hohlraum drive azimuthal asymmetry from the missing drive beams, the 15 remaining outer quads per side are rearranged to fill the gap, reducing its mode 1 asymmetry by a calculated >100× at all times per view-factor calculations, well below the 0.3% ignition requirement [25].

The backlighters are positioned 7.3 and 8.3 mm from the target and angularly spaced by ∼5° to separate by parallax the two radiographs on the passive detector, an medium sensitivity image plate [26], placed at ∼600 mm from the hohlraum for an average image magnification of ∼75×. The image plate is filtered with 500 μm Cu and 500 μm Al to remove core self-emission and softer backlighter x rays (<40 keV). A Cu stepped filter was used to infer the backlighter x-ray bremsstrahlung slope temperature [21]. A series of preliminary radiographs of static W spheres were used to reconstruct the backlighter point spread function, using the method described in Ref. [21], thus enabling better effective resolution by deconvolution of the raw radiographs. The measured backlighter temporal and spatial resolution closely match the laser pulse duration and wire diameter.

Using 25-μm-diameter Au backlighter wires we recorded two radiographs at BT − 10 ps and BT + 160 ps, shown in Fig. 2 after deconvolving the backlighter source. On a

FIG. 1. The experimental setup.
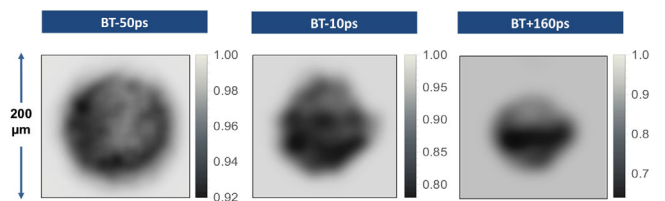

FIG. 2. Compton radiographs of cryogenic THD layered implosion, at BT − 50 ps, BT − 10 ps, and BT + 160 ps.
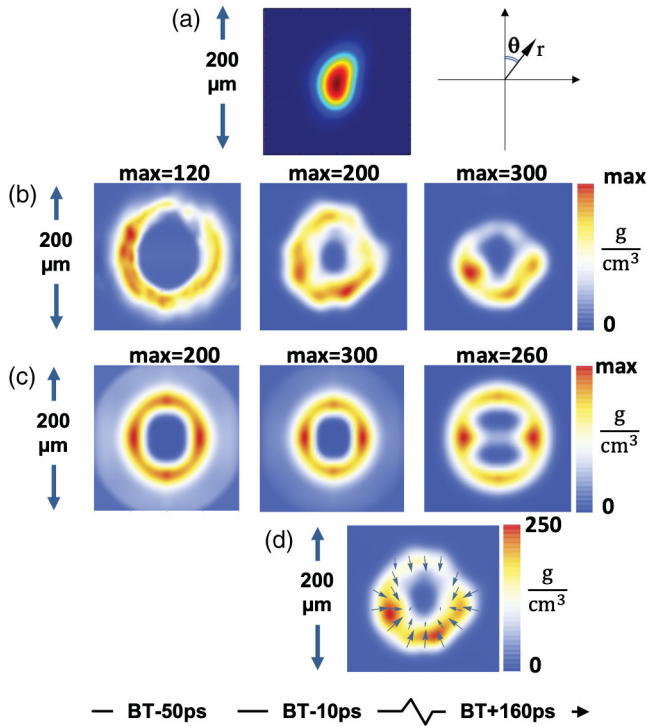
FIG. 3. (a) Left: Primary neutron image at BT; right: coordinate system; (b) evolution of shell density reconstructed from Compton radiographs; and (c) from 2D simulations, including source size and temporal blur; (d) interpolated density and momentum field between BT − 10 ps and BT + 160 ps.
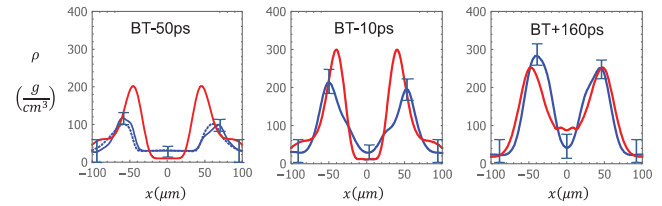

FIG. 4. Solid lines: equatorial lineouts of density from data (blue, with error bars) and from simulations (red). Dashed line: 45° lineout of density from data 50 ps prior bang time.

second shot, a 10-μm Au wire was used, generating the third BT − 50 ps radiograph in Fig. 2. The timing uncertainty is 40 ps relative to the bang time of 7.60 ns, measured by an x-ray streak camera [27]. The unattenuated signal-to-noise (SNR) ratio per resolution element is between 160 and 200. The density, shown in Fig. 3(b), is reconstructed by a forward unfolding procedure, in the 3D cylindrical coordinates of the hohlraum, assuming front-rear symmetry, but allowing left-right asymmetry. The backlighter source point spread function is included in the forward fit algorithm, to avoid possible artifacts that deconvolution of raw radiographs might introduce.

Figure 3(b) shows that the inner profile of the reconstructed fuel near BT is conformal with the burn-weighted primary neutron image (13–17 MeV) of the hot spot in Fig. 3(a) [11]. Figures 3(b) and 3(c) compare the density unfolded from Compton radiographs to the density unfolded from full-integrated 2D simulations at the corresponding times and including source size and 30-ps temporal blur, performed using the HYDRA radiation hydrodynamics code [28]. The data and simulations agree on the presence of greater shell density at the equator than at 45° diagonals. In addition, the data exhibit a thin spot near the north pole, attributable to a residual mode 1 drive imbalance [25]. The direction and magnitude of this mode 1 areal density asymmetry at BT [Fig. 3(b), center], $-(10 \pm 1)\%$

(i.e., bottom-heavy shell) is consistent with the $-(12 \pm 2)\%$ mode 1 inferred using an array of neutron time-of-flight detectors from the neutron downscattered fraction vs angle upon exiting the fuel [29,30].

Figure 3(d) shows the reconstructed momentum field, obtained by differencing between the BT − 10 ps and BT + 160 ps images recorded on the same implosion. The reconstruction is possible because the relative position of the two radiographs is known to better than 2 μm using penumbra images of the two backlighter sources cast by a 3×3 array of apertures in-line with the radiography line of sight. The momentum field assumes no overtaking (mixing) of elements nor azimuthal motion, likely small as no strong azimuthal mode 1 visible.

The density profiles on Fig. 3 show the evolution of the density asymmetry through peak compression, with the density progressively accumulating on the bottom hemisphere. The equatorial lineouts in Fig. 4 show, in contrast to the 2D simulations, a reconstructed density with lower peak, less steep inner profile, and thicker shell near BT, evidence of less fuel compression than expected, as also shown in Figs. 5(c) and 5(d). This discrepancy persists when comparing to 1D simulations or 2D simulations that include a P_1 asymmetry of similar magnitude as observed. Hence, we posit that the less steep inner profiles, as compared to simulations, are due to hydroinstability growth of 3D bubbles and spikes at the fuel-hot-spot interface [31]. The higher-mode density nonuniformities apparent in the reconstruction of the limb in Fig. 3(b) are a further indicator of such perturbations. Figures 5(a) and 5(b) show that while the average radius and equatorial areal density near BT could match the data by invoking 40 ps level cross timing error, no timing offset could make the 2D simulations in Figs. 5(c) and 5(d) match the observed lower peak density, thicker shell. We note that simulations including a P_1 show the same qualitative behavior as the top-down symmetric 2D simulations, therefore still in disagreement with the data. We also note that the 45° lineout (dashed line in Fig. 4) for the early radiograph, still relatively unaffected by the onset of mode-1 asymmetry, is very similar to the equatorial lineout, as are the corresponding metrics (open circles in Fig. 5). Therefore, the departure from 1D behavior cannot be explained simply by the onset of asymmetries.
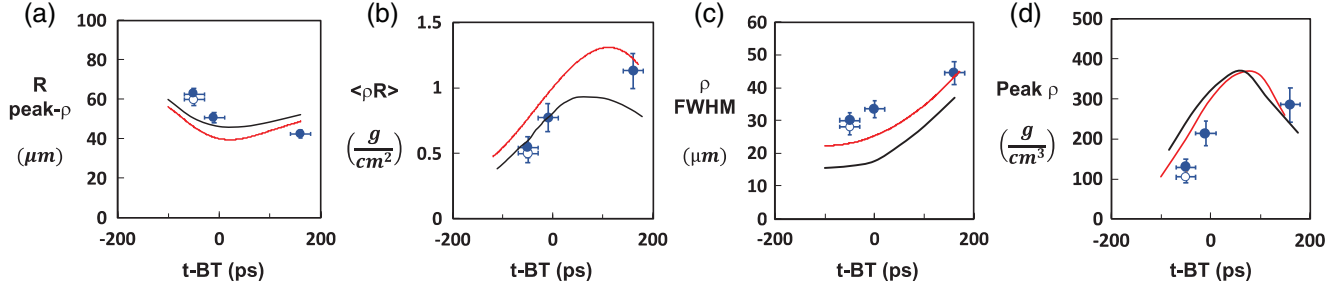
FIG. 5.   Average equatorial metrics vs time, corresponding to lineouts from Fig. 4 of density unfolded from data radiographs (solid blue dots) compared to simulations directly (1D, black lines) and unfolded from simulated radiographs (2D, red lines). (a) Radius at peak density; (b) areal density; (c) density FWHM; (d) peak density. In all figures: open circles represent metrics from 45° lineout from Fig. 4, at BT − 50 ps.

The accuracy in inferring density can be estimated from error propagation applied to the equation for areal density $\rho\Delta R$: $\rho\Delta R = \ln(1/T)/\kappa_{KN}$, where T is the transmission, ΔR is the thickness of the density distribution, and $\kappa_{KN} = 0.3\ Z/A\ cm^2/g$ is the average effective opacity due to fuel Compton scattering of the 50–200 keV photons that make up most of the signal. Table I lists the sources of uncertainties and their estimated values that added in quadrature yield a local peak density accuracy of 13%–15%. The inferred total mass for the central frame $=160 \pm 14\ \mu g$, larger than the 110 μg of initial TH mass, consistent with some ablator remaining in field of view. Since the absolute error in the hot-spot and fuel areal density which share the same line of sight are correlated and comparable, the uncertainty in the much lower hot-spot density is proportionally larger, effectively 100%, as reflected in Fig. 4.

Having two radiographs on the same shot provides previously unattainable insight into the dynamics of the fuel trajectory and in particular its kinetic energy. The near shape sphericity suggests the kinetic energy (K_{res}) can then be separated into an easily calculable radial component $1/2M(\Delta r_c/\Delta t)^2$ of center-of-mass radius r_c and rotational

component $\frac{1}{2}\int m\omega^2 r_c^2 d\theta$, where we have further assumed no azimuthal areal density variations (cylindrical symmetry). The angular velocity $\omega(\theta)$ and annular mass $m(\theta,t)d\theta = 2\pi r_c(t)^2 \sin\theta d\theta \int \rho(r,\theta,t)dr$ are linked through the spherical surface continuity equation $dm(\theta)/dt = -d[m(\theta)\omega(\theta)]/d\theta$. We can expand $m(\theta,t)$ in Legendre modes $P_n(\theta,t)$ and solve mode by mode, yielding, to zeroth order, a rotational kinetic energy $K_{rot} = \frac{1}{2}\langle Mr_c^2\rangle\Sigma[\Delta(P_n/P_0)/\Delta t]^2/[n(n+1)(2n+1)]$ that excludes the unlikely scenario of a spinning fuel. This equation has been verified by synthetic simulations. In practice, the reconstruction provides left and right contributions that are calculated separately and summed. This gives 3% more K_{rot} than if just used left-right averaged Legendre modes, justifying the assumption that the contribution of low-mode azimuthal variations is small. Plugging in experimental values for the shell radial compression $\Delta r_c = -11 \pm 0.3\ \mu m$, average moment of inertia of the two frames $\langle Mr_c^2\rangle = 0.39 \pm .04\ g\,\mu m^2$, modal mass changes $\Delta(P_n/P_0)$, (-0.33 ± 0.02 for dominant P_1), and temporal separation $\Delta t = 170 \pm 15$ ps whose error dominates, we find that the total BT kinetic energy $K_{res} = 450 \pm 90$ J, of which $(27 \pm 2)\%$ is

TABLE I.   Sources of relative uncertainty for the density. (a) Uncertainty in transmission T, where $\delta T/T = \sqrt{2}/$SNR, SNR being the signal-to-noise ratio; α is a multiplier from propagating uncertainties during data unfold, between 1 to 1.4, increasing as SNR decreases. (b) Klein-Nishina systematic cross section uncertainty due to the slope temperature uncertainty of the backlighter spectrum. (c) Systematic shell thickness uncertainty dominated by uncertainty in the backlighter source size. (d) Systematic uncertainty due to the average background-to-signal ratio δBSR uncertainty at limb minimum. (e) Uncertainty in the unattenuated flux level I_0 given the finite field-of-view $\approx 2x$ the fuel radius. (f) and (g) uncertainty in mixed opacity from uncertainty in the amount of ablator (of Compton opacity $(Z/A)_C = 1.25(Z/A)_{TH}$) and W dopant (of opacity κ_W) mix into the fuel, estimated from simulations at 0–30 μg of C and 0–0.1 μg of W in the 110 μg of 75:25 TH fuel.

(a) Transmission	$[\alpha/Ln(T)]\delta T/T$	2%–7%
(b) Klein-Nishina cross section	$\delta\sigma_{KN}/\sigma_{KN}$	2%
(c) Shell thickness	$\delta\Delta R/\Delta R$	6%–7%
(d) Background-to-signal	$[(1-T)\delta BSR/Ln(T)]$	11%–13%
(e) Unattenuated flux	$\approx(1/\sqrt{5})[1/Ln(T)](\delta I_0/I_0)$	3%–8%
(f) C ablator mix	$0.25\delta\rho_C/\rho_{TH}$	3%
(g) W dopant mix	$[(\kappa_W - \kappa_{KN})\delta\rho_W/\kappa_{KN}\rho_{TH}]$	2%

rotational P_1 and $(1 \pm 1)\%$ is rotational P_2 and P_3. Additional contributions from shell mode 1 translational and P_2 and P_3 radial kinetic energy are $\approx 1.5\%$ each, validating the sphere shape approximation. Moreover, the measured low level of shell P_1 translational velocity $(-2 \pm 12 \ \mu\text{m/ns})$, modest BT 11% P_1 areal density nonuniformity yet significant measured $60 \pm 15 \ \mu\text{m/ns} \ P_1$ hot spot velocity extracted from time-of-flight neutron spectroscopy [32] are all self-consistent with current and published simulation predictions [33] for the case of a plausible 0.5% P_1 peak flux asymmetry. There is one further source of residual kinetic energy, the peristaltic or energy of shell profile stretching or compression, where the ratio peristaltic-to-radial K_{rad} is given approximately by $(\Delta\Delta R/\Delta r_c)^2/12$. Since Figs. 5(a) and 5(c) show Δr_c and ΔR are both about 11 μm between the two frames at the equator which contains most but not all the mass, we indeed calculate this ratio to be less than 1/12, so < 25 J of stretching energy.

It is now instructive to compare the residual BT kinetic energy (K_{res}) to the kinetic energy $1/2Mv_i^2$ at peak fuel velocity, $v_i = 350 \pm 15 \ \mu\text{m/ns}$, derived from conventional 1D radiography [34]. Any unconverted kinetic energy represents a loss to the internal energy of the hot spot and hence yield. The ratio is $1.3 \pm 0.3\%$ for the P_1 component that compares well to a simulated 1.4% assuming as above a 0.5% P_1 asymmetry. However, the remainder of the inferred K_{res} of $3.7 \pm 1\%$, due to the decreasing average radius, is both qualitatively and quantitatively in contrast to simulations that predict an increase in radius after bang time, with minimum K_{res} fraction of 0.03%, in the case of 1D simulation, rising to 1.5%, in the case of 2D simulation, principally due to asynchrony in pole vs equator trajectory. This total $5 \pm 1\%$ level of K_{res} should degrade yield to 0.75 ± 0.05 of clean-simulated yield (Y_{oC}), according to models [35,36] backed by simulations giving $Y_{\text{oC}} = (1 - K_{\text{res}})^{5.5}$. We note that four companion DT implosion experiments performed using the same three-shock high-density carbon platform have resulted in an average $Y_{\text{oC}} \sim 0.65 \pm 0.10$. Our measurement therefore shows that the residual kinetic energy is a significant contributor to yield degradation.

In summary, we have used 30-ps and 10-μm resolution Compton radiography to provide direct imaging of the stagnating inertial confinement fusion fuel and remaining ablator and reconstruction of the fuel density evolution. We have measured the degree of fuel compression and nonuniformities, as well as the undesirable residual kinetic energy at peak compression, the main parameters impacting implosion efficiency and confinement. Our first data show thicker fuel, with lower peak density than predicted by simulations, suggesting a higher stagnated adiabat and unresolved higher-mode instability growth. The presence of mode 1 fuel nonuniformity inferred from burn integrated neutron scattering has been confirmed.

The differencing of two sequential Compton radiographs allows the inference of the momentum field and shows that the amount of residual kinetic energy corresponding to both radial and low modes rotational energy of the fuel can explain much of the observed reduction in yield compared to 1D simulations.

---

*Corresponding author.
tommasini2@llnl.gov

[1] J. Lindl, Phys. Plasmas **2**, 3933 (1995).
[2] O. A. Hurricane *et al.*, Plasma Phys. Controlled Fusion **61**, 014033 (2018).
[3] R. Betti, P. Y. Chang, B. K. Spears, K. S. Anderson, J. Edwards, M. Fatenejad, J. D. Lindl, R. L. McCrory, R. Nora, and D. Shvarts, Phys. Plasmas **17**, 058102 (2010).
[4] G. Miller, E. Moses, and C. Wuest, Nucl. Fusion **44**, S228 (2004).
[5] J. Meyer-ter-Vehn, S. Atzeni, and R. Ramis, Europhysics News **29**, 202 (1999).
[6] M. Murakami and J. Meyer-ter-Vehn, Nucl. Fusion **31**, 1315 (2011).
[7] G. P. Grim *et al.*, Phys. Plasmas **20**, 056320 (2013).
[8] D. T. Casey, P. L. Volegov, F. E. Merrill, D. H. Munro, G. P. Grim, O. L. Landen, B. K. Spears, D. N. Fittinghoff, J. E. Field, and V. A. Smalyuk, Rev. Sci. Instrum. **87**, 11E715 (2016).
[9] L. Divol *et al.*, Phys. Plasmas **24**, 056309 (2017).
[10] C. B. Yeamans, D. L. Bleuel, and L. A. Bernstein, Rev. Sci. Instrum. **83**, 10D315 (2012).
[11] P. Volegov, C. R. Danly, D. N. Fittinghoff, G. P. Grim, N. Guler, N. Izumi, T. Ma, F. E. Merrill, A. L. Warrick, C. H. Wilde, and D. C. Wilson, Rev. Sci. Instrum. **85**, 023508 (2014).

[12] P. L. Volegov, S. H. Batha, V. Geppert-Kleinrath, C. R. Danly, F. E. Merrill, C. H. Wilde, D. C. Wilson, D. T. Casey, D. Fittinghoff, B. Appelbe, J. P. Chittenden, A. J. Crilly, and K. McGlinchey, J. Appl. Phys. **127,** 083301 (2020).

[13] N. B. Meezan et al., Plasma Phys. Controlled Fusion **59,** 014021 (2016).

[14] R. Tommasini, S. P. Hatchett, D. S. Hey, N. Izumi, J. A. Koch, O. L. Landen, A. J. Mackinnon, J. A. Delettrez, V. Y. Glebov, T. C. Sangster, and C. Stoeckl, Phys. Plasmas **18,** 056309 (2011).

[15] O. Klein and Y. Nishina, Z. Phys. **52,** 853 (1929).

[16] P. Nozieres and D. Pines, Theory of Quantum Liquids (WA Benjamins, New York, 1966).

[17] T. Doppner et al., Phys. Rev. Lett. **121,** 025001 (2018).

[18] A. B. Zylstra et al., Phys. Plasmas **22,** 056301 (2015).

[19] L. Berzak Hopkins, L. Divol, C. Weber, S. Le Pape, N. B. Meezan, J. S. Ross, R. Tommasini, S. Khan, D. D. Ho, J. Biener, E. Dewald, C. Goyon, C. Kong, A. Nikroo, A. Pak, N. Rice, M. Stadermann, C. Wild, D. Callahan, and O. Hurricane, Phys. Plasmas **25,** 080706 (2018).

[20] M. J. Edwards, J. D. Lindl, and B. K. Spears, Phys. Plasmas **18,** 051003 (2011).

[21] R. Tommasini et al., Phys. Plasmas **24,** 053104 (2017).

[22] J.-M. G. Di Nicola et al., in Proc. SPIE, edited by A. A. S. Awwal and M. A. Lane (2015), pp. 93450I–1.

[23] J. E. Heebner et al., Appl. Opt. **58,** 8501 (2019).

[24] H. Chen et al., Phys. Plasmas **24,** 033112 (2017).

[25] C. V. Young, L. Masse, D. T. Casey, B. J. MacGowan, O. L. Landen, D. A. Callahan, N. B. Meezan, R. Nora, and P. K. Patel, Phys. Plasmas **27,** 082702 (2020).

[26] N. Izumi, R. Snavely, G. Gregori, J. A. Koch, H. S. Park, and B. A. Remington, Rev. Sci. Instrum. **77,** 10E325 (2006).

[27] S. F. Khan et al., Proc. SPIE **8505,** 850505 (2012).

[28] M. M. Marinak, S. W. Haan, T. R. Dittrich, R. E. Tipton, and G. B. Zimmerman, Phys. Plasmas **5,** 1125 (1998).

[29] R. Hatarik, J. A. Caggiano, V. Glebov, J. McNaney, C. Stoeckl, and D. H. G. Schneider, Plasma Fusion Res. **9,** 4404104 (2014).

[30] R. Hatarik, R. C. Nora, B. K. Spears, M. J. Eckart, G. P. Grim, E. P. Hartouni, A. S. Moore, and D. J. Schlossberg, Rev. Sci. Instrum. **89,** 10I138 (2018).

[31] A. Bose, R. Betti, D. Shvarts, and K. M. Woo, Phys. Plasmas **24,** 102704 (2017).

[32] H. G. Rinderknecht, D. T. Casey, R. Hatarik, R. M. Bionta, B. J. MacGowan, P. Patel, O. L. Landen, E. P. Hartouni, and O. A. Hurricane, Phys. Rev. Lett. **124,** 145002 (2020).

[33] B. K. Spears, M. J. Edwards, S. Hatchett, J. Kilkenny, J. Knauer, A. Kritcher, J. Lindl, D. Munro, P. Patel, H. F. Robey, and R. P. J. Town, Phys. Plasmas **21,** 042702 (2014).

[34] D. G. Hicks et al., Phys. Plasmas **19,** 122702 (2012).

[35] A. L. Kritcher, R. Town, D. Bradley, D. Clark, B. Spears, O. Jones, S. Haan, P. T. Springer, J. Lindl, R. H. H. Scott, D. Callahan, M. J. Edwards, and O. L. Landen, Phys. Plasmas **21,** 042708 (2014).

[36] K. M. Woo, R. Betti, D. Shvarts, O. M. Mannion, D. Patel, V. N. Goncharov, K. S. Anderson, P. B. Radha, J. P. Knauer, A. Bose, V. Gopalaswamy, A. R. Christopherson, E. M. Campbell, J. Sanz, and H. Aluie, Phys. Plasmas **25,** 102710 (2018).